Chinese Chemical Letters 34 (2023) 107855

Contents lists available at ScienceDirect

Chinese Chemical Letters

journal homepage: www.elsevier.com/locate/cclet

# Facile preparation of hierarchical Ni@Mn-doped NiO hybrids for efficient and durable oxygen evolution reaction

Yi Liu[a,*], Liang Bai[a], Qiqi Jia[a], Peitong Li[a], Yao Yan[a], Ningkai Yuan[a], Xiaodong Hao[b,*]

[a] School of Materials Science and Engineering, Shaanxi Key Laboratory of Green Preparation and Functionalization for Inorganic Materials, Institute of Frontier Science and Technology Transfer, Shaanxi University of Science and Technology, Xi'an 710021, China
[b] Materials Institute of Atomic and Molecular Science, Shaanxi University of Science and Technology, Xi'an 710021, China

ARTICLE INFO

*Article history:*
Received 11 June 2022
Revised 1 September 2022
Accepted 23 September 2022
Available online 25 September 2022

*Keywords:*
Core-shell structure
OER
Electrocatalysis
Water splitting
First principle calculation

ABSTRACT

Exploring highly efficient and non-noble-metal-based electrocatalysts for oxygen evolution reaction (OER) is of great importance not only for water splitting but also for rechargeable metal-air batteries and fuel cells. Herein, we describe a simple strategy to prepare hierarchical Ni@Mn-doped NiO hybrids using flower-like Ni-Mn layered double hydroxides (NiMn-LDHs) as a precursor. After calcination at 400 °C for an hour under $N_2$ atmosphere, the flower-like NiMn-LDHs transform to porous microspheres consisting of nanoparticles, in which Ni cores are encapsulated by Mn-doped NiO shells (denoted as Ni@Mn-NiO-400). Benefiting to this unique porous, core-shell structures and element doping, the as-prepared Ni@Mn-NiO-400 hybrid shows a low overpotential of 178 mV at the current density of 10 mA/cm$^2$ and Tafel slope of 52.7 mV/dec in 1 mol/L KOH solution. More significantly, the Ni@Mn-NiO-400 hybrid also demonstrates superior stability of 98.6% after 50 h continuously testing, much higher than pristine NiMn-LDHs and commercial $IrO_2$ catalyst. In addition, theoretical simulation shows that Ni core and Mn doping greatly affect the electronic states and electronic structure of NiO. As a result, Ni@Mn-doped NiO hybrid possesses an optimal adsorption activity towards oxygen species than NiO and undoped Ni@NiO hybrid. Considering the compositional and structural flexibility of LDHs, this work may offer a simple method to prepare other non-noble metal-based electrocatalysts for OER.

Hydrogen production *via* electrocatalytic water splitting is a renewable and environmentally friendly method of energy storage and conversion [1–3]. The oxygen evolution reaction (OER), an important half-reaction in electrocatalytic water splitting, involves complex reaction intermediates and is related to the formation of oxygen-oxygen bonds *via* four proton-coupled electron transfers [4–6]. So it is kinetically sluggish and usually needs the assistance of electrocatalysts to accelerate the reaction, reduce the overpotential, as well as boost the energy conversion efficiency [7–9]. Although precious metals and their oxides (for example, $RuO_2$ and $IrO_2$) exhibit good electrocatalytic capacities, the high-cost and lack of supply restrict their actual utilization [10–12]. Therefore, the search for efficient and non-noble-metal-based electrocatalysts has attracted extensive attention in these years [13,14]. Until now, plenty of electrocatalysts, such as perovskites oxides [15,16], chalcogenide [17], transition metal oxides/hydroxides/oxyhydroxides [18,19], and phosphates [20], have been extensively investigated. Among them, transition metal oxides especially NiO is recognized as prospective candidates for OER catalysts owing to its enrichment, low cost, good corrosion resistance, and comparatively low overpotential. Nevertheless, the oxygen-evolving performance of pure NiO is limited since the poor conductivity and less active sites [21].

To overcome this obstacle, tremendous efforts have been devoted in last years. For instance, NiO microspheres or nanocrystals (2.5∼5 nm) with core-shell structures, high specific surface areas, as well as 2D nanosheet-like shells were synthesized [22,23], which led to the modulation in surface properties and augment in electrocatalytic active sites. The porous and hierarchical structures greatly promote charge transport and reduce ion transport pathways. Furthermore, the preparation of NiO on the three-dimensional (3D) conductive substrates is another way to increase the conductivity [24,25]. For example, the NiO nanosheets on 3D interconnected pristine graphene were prepared by an *in-situ* self-assembly method [25], which provided facile accesses to the cat-

---

* Corresponding authors.
*E-mail addresses:* liuyi@sust.edu.cn (Y. Liu), hao.xiaodong@sust.edu.cn (X. Hao).

https://doi.org/10.1016/j.cclet.2022.107855

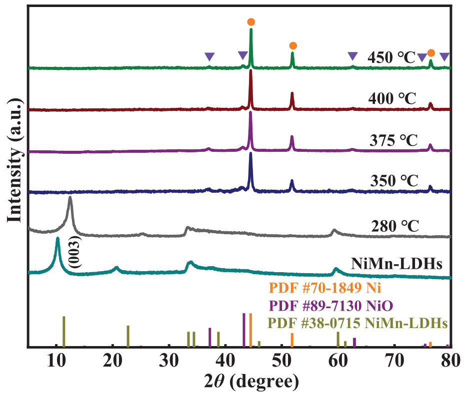

**Fig. 1.** XRD patterns of NiMn-LDHs and its calcined products.

alytically active sites and a fast electron conducting network for charge transport. In addition, the heterostructures (*e.g.,* Ni/NiO, NiO/NiS, NiO/$Cr_2O_3$ and NiO/$CeO_2$) can also facilitate the charge separation and electron transfer in the process of electrocatalytic reaction, and thus improving the catalytic activity [26–30]. Besides, element doping can also increase the catalytic activities [31–34]. For example, incorporation of Fe into NiO lattice can create the beneficial active surface phases, resulting in the improved catalytic activities at a specific potential [31]. As mentioned above, decreasing grain sizes, creating porous and hierarchical structures, involving core-shell structures, and introducing foreign elements are all effective strategies for improving the oxygen-evolving performance of NiO. It is expected that the oxygen-evolving performance can be further improved once these strategies are adopted simultaneously. Nevertheless, the synthesis method to achieve this expectation still remains challenging.

In this work, we describe a simple strategy to synthesize Ni@Mn-doped NiO microspheres which have porous and core-shell structures combined with nanocrystals and element doping. To do it, flower-like NiMn-LDHs are prepared firstly *via* a facile hydrothermal method and subsequently calcined at different temperatures under $N_2$ atmosphere. The microstructure and electrocatalytic performance for OER of the as-obtained products are systematically investigated. For comparison, the undoped Ni@NiO microspheres are also prepared and the effect of Mn doping is also elaborated. In addition, the electronic structure and adsorption properties of the catalysts are studied by first principle calculation based on density functional theory (DFT). The detailed experimental process, material characterization, and calculation parameters are described in the supporting information.

Fig. 1 displays the X-ray diffraction (XRD) patterns of as-prepared NiMn-LDHs and its calcined products. It can be seen that the principal phases still remain to LDHs as the calcination temperatures are increased to 280 °C, even though the diffraction peaks of (003) plane shift to larger angles, reflecting a reduction in interlayer space. The reason for angular shifts lies in the evaporation of water between LDHs layers, and which is of consistence within the thermal gravity (TG) curves of NiMn-LDHs (Fig. S1 in Supporting information). When the calcination temperatures exceed 350 °C, merely pure Ni and NiO phases are existent in the final-products, which means that the occurrence of the thorough dehydration as well as phase decomposition of NiMn-LDHs. According to the relative intensities of diffraction peaks, it can be found that the obtained products are mainly composed of pure Ni substance and a small amount of NiO. There are no extra diffraction peaks detected from all calcined products, demonstrating clearly that the Mn-based oxides are not generated during calcining process. Furthermore, the fourier transform infrared (FTIR) spectra of NiMn-LDHs and the calcined products were also acquired (Fig. S2 in Supporting information), well consistent with the XRD and TG analysis described above. For the sake of verifying the existence and the contents of Mn element in NiMn-LDHs and calcined products, the inductively coupled plasma optical emission spectroscopy (ICP-OES) was conducted. As summarized in Table S1 (Supporting information), the atomic ratios of Ni/Mn in NiMn-LDHs as well as calcined products are almost the same (~10:1). The above results confirm that the Mn atoms may possibly get into the crystal lattices of Ni and/or NiO in the course of the decomposition of NiMn-LDHs.

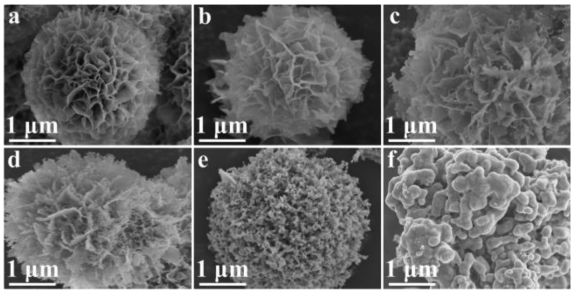

**Fig. 2.** The SEM images of (a) NiMn-LDHs, (b) Ni@Mn-NiO-280, (c) Ni@Mn-NiO-350, (d) Ni@Mn-NiO-375, (e) Ni@Mn-NiO-400, and (f) Ni@Mn-NiO-450 hybrid.

The microstructure of the pristine NiMn-LDHs as well as its all calcined products are observed utilizing scanning electron microscopy (SEM). As displayed in Figs. 2a and b, when the calcination temperatures rise to 280 °C, the flower-like morphology still remains, which means that no decomposition occurs. Nevertheless, tiny nanoparticles appear at the margin of the floral sheets (Fig. 2c) as the calcination temperatures are increased to 350 °C, indicating that NiMn-LDHs are beginning to decompose. When the calcination temperatures are increased to 375 °C, the number of nanoparticles appearing at the edge of the floral sheets further increases (Fig. 2d). As the calcination temperatures further rising, floral sheets vanished step by step, and transformed into nanoparticles at 400 °C. All findings are of coincidence within XRD and FTIR analysis. Hence, porous microspheres composed of nanoparticles are obtained (Fig. 2e). In this case, the Brunauere Emmette Teller (BET) specific surface of Ni@Mn-NiO-400 hybrid achieves 65.2 $m^2$/g that is greater than that of other calcined products as compared in Fig. S3a (Supporting information). Besides, the Barrett-Joyner-Halenda (BJH) pore size distribution curves in Fig. S3b (Supporting information) demonstrate that Ni@Mn-NiO-400 hybrid possesses two diverse types of pore sizes, 8–18 and 20–40 nm, respectively. Furthermore, the grain growth takes place as the calcination temperatures rise to 450 °C, and thus giving rise to the reduction of the specific surface areas (Fig. 2f and Fig. S3a). The high-resolution transmission electron microscopy (HRTEM) and energy dispersive X-ray spectroscopy (EDS) of the calcined samples are carried out and the images are exhibited in Figs. S4 and S5 (Supporting information). Obviously, the four samples have similar microstructure and, the elemental EDS mappings reveal that Ni, Mn, and O exist in the corresponding catalysts. However, the specific distribution of Ni and NiO phases, as well as the elemental distribution of Mn atoms are still unclear.

For the sake of providing more sufficient evidence, the Ni@Mn-NiO-400 hybrid as a representative sample is characterized utilizing aberration-corrected scanning transmission electron microscopy (Ac-STEM). As shown in Fig. 3a, the aberration-corrected high angular annular dark-field scanning transmission electron microscopy (HAADF-STEM) images and corresponding elemental EDS mappings demonstrate that Ni mainly distributes in the internal of catalysts, the minority of Mn and O disperses in the external

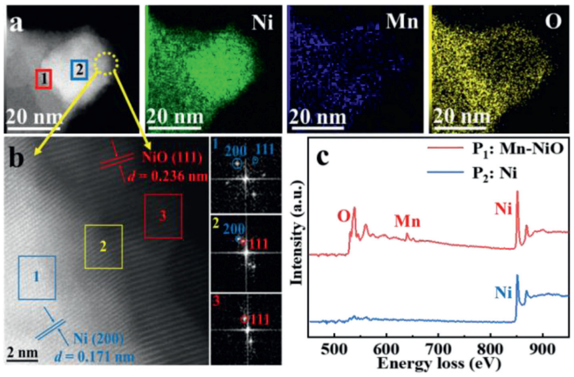

**Fig. 3.** (a) The elemental EDS mappings of Ni@Mn-NiO-400 hybrid: ADF image, followed *via* the separate mappings of Ni, Mn and O, respectively. The EELS spectra acquisition area is shown by the rectangular boxes in the ADF image of (a). (b) HAADF-STEM image and the corresponding selective area FFT patterns of Ni@Mn-NiO-400 hybrid. (c) EELS spectra of acquisition area.

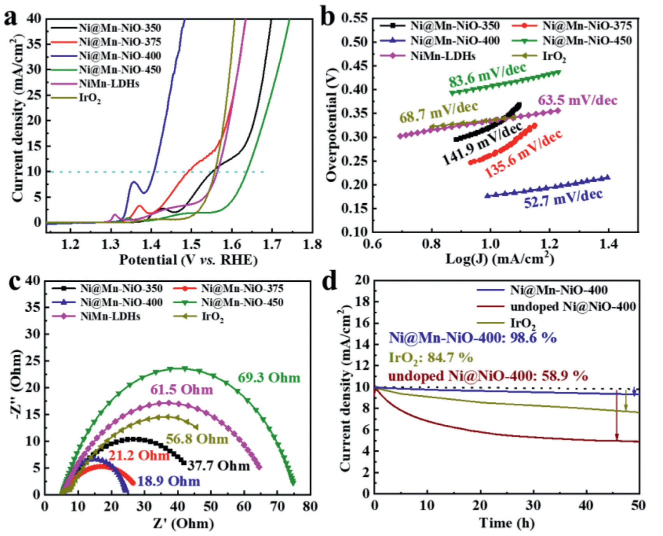

**Fig. 4.** The oxygen-evolving performance of pristine NiMn-LDHs, Ni@Mn-doped NiO hybrids, as well as commercial $IrO_2$ catalyst. (a) OER linear sweep voltammetry (LSV) curves within iR-corrected, (b) Tafel plots generated from LSV curves in (a), (c) EIS Nyquist plots, (d) long-term stability estimation of diverse catalysts at given potential of 1.41, 1.50 and 1.56 V *vs.* RHE, respectively.

of the nanoparticles, indicative of the possible formation of core-shell structure. Moreover, the high-resolution HAADF-STEM image and the corresponding selective area fast-Fourier transform (FFT) patterns in Fig. 3b show a clear two phases of Ni and NiO, and the lattice fringe distances of ~0.171 and ~0.236 nm can be indexed to the Ni (200) and NiO (111) crystal plane, respectively. The electron energy loss spectrum (EELS) spectra data were acquired at two positions of Ni@Mn-NiO-400 hybrid as shown in Fig. 3a, and it shows in Fig. 3c that the major signals of $Ni^{2+}$ ($L_{2,3}$ edge: 873.6 and 855.7 eV), $Mn^{3+}$ ($L_{2,3}$ edge: 649.7 and 638.5 eV), and O (K edge: 538.9 eV) can be obtained in periphery of nanoparticles [35,36], but it appears only the signal of $Ni^0$ ($L_{2,3}$ edge: 869.3 and 851.5 eV) inside the nanoparticles [37,38], illustrating the formation of the Ni cores and Mn-doped NiO shells. In comparing with previous literature [35–38], it should be noted that minor shifts to higher energy loss are observed in $Ni^{2+}$ $L_{2,3}$ whereas $Mn^{3+}$ $L_{2,3}$ exhibits slight shifts to lower energy loss, indicative of the existence of the electron transfer (Ni → Mn), well consistent with the X-ray photoelectron spectroscopy (XPS) characterization analysis results (Fig. S6 in Supporting information).

The oxygen-evolving performances of the Ni@Mn-doped NiO hybrids, NiMn-LDHs precursor, and commercial $IrO_2$ catalyst were evaluated in $O_2$-saturated 1.0 mol/L KOH solution (pH 13.8, RT) utilizing routine three-electrode systems. The Ni@Mn-NiO-400 hybrid exhibits that only 178 mV (overpotential *vs.* reversible hydrogen electrode (RHE)) is needed to achieve catalytic current density of 10 mA/cm$^2$ (Fig. 4a and Fig. S7a in Supporting information) within a small Tafel slope of 52.7 mV/dec (Fig. 4b); relatively high mass activity (223.93 mA/mg) is reflected at a given potential of 1.50 V *vs.* RHE (Fig. S7b in Supporting information). These results are superior to other calcined samples, NiMn-LDHs precursor, as well as commercial $IrO_2$ catalyst, showing the outstanding electrocatalytic performance, fast kinetics, and substantial activity of Ni@Mn-NiO-400 hybrid in the OER process. Meanwhile, the Ni@Mn-NiO-400 hybrid shows also the minimum overpotential and competitive Tafel slope in comparing with non-noble-metal Ni-based catalysts reported at present (Fig. S7e and Table S2 in Supporting information). The double layer capacitance ($C_{dl}$) calculated from the cyclic voltammetry (CV) curves (Fig. S8 in Supporting information) of the Ni@Mn-NiO-400 hybrid was 0.152 mF/cm$^2$, which is larger than that of other calcined samples, NiMn-LDHs precursor, and commercial $IrO_2$ catalyst (Fig. S7c and Table S3 in Supporting information), indicating that the Ni@Mn-NiO-400 hybrid possesses larger electrochemical surface areas and can expose more active sites in driving water oxidation. This is supported *via* the BET specific surface area of all calcined products (Fig. S3a). The excellent electrochemical properties of the Ni@Mn-NiO-400 hybrid are due most probably to its distinctive core-shell and porous structure, in which the smaller pores are easy to capture intermediates (OH*, O* and OOH*), while the larger pores facilitate the penetration of electrolyte solution into the whole structure.

The electrochemical impedance spectroscopy (EIS) was also studied to further understand the electrocatalytic kinetics for OER. Obviously, the Ni@Mn-NiO-400 hybrid possesses relatively small charge transfer resistances ($R_{ct}$, *ca.* 18.9 Ohm) corresponding to other calcined samples, pristine NiMn-LDHs, and commercial $IrO_2$ catalyst (Fig. 4c and Table S4 in Supporting information), indicative of the faster electron transportation efficiency, and thus enhancing the OER performance. To better comprehend the effect of Mn doping on the oxygen-evolving performances, the catalytic properties of undoped Ni@NiO hybrid with the similar microstructure (Fig. S9a in Supporting information), were elaborated. It can be concluded from Fig. S10 (Supporting information) that the electrocatalytic capacity towards OER of Ni@NiO hybrid can be enhanced by Mn doping. Furthermore, the turnover frequency (TOF) value of Ni@Mn-NiO-400 hybrid is approximately twice that of undoped Ni@NiO-400 hybrid and 14 times that of commercial $IrO_2$ catalyst, at a given potential 1.56 V *vs.* RHE (Fig. S7d in Supporting information). Evidently, Ni@Mn-NiO-400 hybrid possesses the faster reaction rate over those of the undoped Ni@NiO-400 hybrid and commercial $IrO_2$ catalyst. More importantly, after 50 h of cycle for stability testing, the current density of the Ni@Mn-NiO-400 hybrid can be still maintained at 98.6% (Fig. 4d), and the structural morphology is also preserved well (Fig. S11 in Supporting information), reflecting the great durability.

The above experimental data have revealed that the Ni@Mn-NiO-400 hybrid has excellent catalytic activities for OER owing to the distinctive hierarchical structure and Mn doping. In order to comprehend the intrinsic mechanism deeply, electronic structure and adsorption activity to oxygen species of NiO, Ni@NiO, and Ni@Mn-NiO were estimated theoretically utilizing DFT+U method based on VASP software. The theoretical model of catalysts are shown in Fig. S12 (Supporting information). Fig. 5a displays the charge density difference distributions of Ni@Mn-NiO, where the green and yellow areas stand for electron depletion as well as accumulation, respectively. Apparent electron accumulation and de-

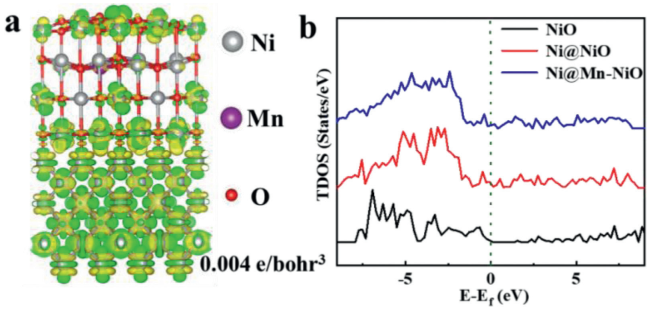

**Fig. 5.** (a) The yellow and green colors describe electron accumulation and depletion, respectively, in the differential charge density distributions of Ni@Mn-NiO. The isosurface value is set to 0.004 e/bohr$^3$. (b) Curves of total density of states (TDOS) for NiO, Ni@NiO, and Ni@Mn-NiO, respectively.

pletion are observed on catalysts, showing charge accumulation at the interface and transfer from NiO to Ni. This electronic configuration caused by charge transfer is conducive to electrocatalytic OER process, especially, the potential barrier of the rate determining step (RDS) in the OER process can be reduced, which has been confirmed in our previous work [32].

The electronic structure of pure NiO exhibits semiconductor characteristics, as shown in total densities of electronic states (Fig. 5b), while a certain number of electronic states are observed near the Fermi level after combined Ni core and Mn doping, revealing the enhanced electron mobility as well as a more conductive electronic structure, which is another significant factor for exceptional catalytic activity of Ni@Mn-NiO. The width of D-band ($W_{\mathrm{d}}$) is introduced into the D-band center ($\varepsilon_{\mathrm{d}}$) as an improved reactivity descriptor ($\varepsilon_{\mathrm{u}}$) to evaluate the adsorption activity of the catalysts towards oxygen species [39]. The results show that the $\varepsilon_{\mathrm{u}}$ shifted to $-2.44$ eV for Ni@Mn-NiO from $-3.74$ eV of undoped Ni@NiO and $-6.03$ eV of NiO, which is closer to the Fermi level. This further confirms the Ni core and Mn doping cause the antibonding state to move and empty above the Fermi level, resulting in the increase of bond strength [40]. Thus, the theoretical simulations and experimental studies demonstrate that within unique Ni core and Mn-doped NiO shell, the charge transportation of Ni@Mn-NiO can be enhanced and the electronic structure of active metal sites of the Ni@Mn-NiO are modulated, which optimize significantly the electrocatalytic kinetics as well as enhance the electrocatalytic activity.

In brief, utilizing NiMn-LDHs as precursors, we developed a straightforward strategy for synthesizing Ni@Mn-doped NiO hybrids *via* simply regulating the calcination temperatures. The as-prepared Ni@Mn-doped NiO hybrids were composed of porous microspheres consisting of nanoparticles, in which Ni cores are encapsulated by Mn-doped NiO shells. It is found that Ni@Mn-NiO-400 hybrid exhibits better electrocatalytic performance in alkaline medium, whose overpotential *vs.* RHE is only 178 mV at the current density of 10 mA/cm$^2$ within a Tafel slope of 52.7 mV/dec; more considerably, the current density can be maintained at 98.6% after 50 h of cycle stability testing, indicative of remarkably efficient and stable OER catalysts. The decent oxygen-evolving performances can be ascribed to the unique core-shell structures as well as Mn doping, which improve charge transportation and enlarge catalytically active sites. Ultimately, the work including the synthetic strategy and theoretical calculation may provide a new guideline for developing other non-precious metal-based electrocatalysts for OER.

## Declaration of competing interest

The authors declare that they have no known competing financial interests or personal relationships that could have appeared to influence the work reported in this paper.

## Acknowledgments

This work was supported by National Natural Science Foundation of China (Nos. 51602184 and 21902096), Natural Science Foundation of Shaanxi Province (Nos. 2020JM-505 and 2020JM-502) and the Academic Talent Introduction Program of SUST (No. 134080056).

## Supplementary materials

Supplementary material associated with this article can be found, in the online version, at doi:10.1016/j.cclet.2022.107855.

## References

[1] D.J. Zhou, P.S. Li, X. Lin, et al., Chem. Soc. Rev. 50 (2021) 8790–8817.
[2] L. Lv, Z.X. Yang, K. Chen, C.D. Wang, Y.J. Xiong, Adv. Energy Mater. 9 (2019) 1803358.
[3] K.X. Wang, Y.L. Wang, B. Yang, et al., Energy Environ. Sci. 15 (2022) 2356–2365.
[4] M. Tahir, L. Pan, F. Idrees, X. Zhang, L.W. Zhong, Nano Energy 37 (2017) 136–157.
[5] G. Buvat, M. Eslamibidgoli, A. Youssef, S. Garbarino, D. Guay, ACS Catal. 10 (2020) 806–817.
[6] F.P. Cheng, Z.J. Li, L. Wang, et al., Mater. Horiz. 8 (2021) 556–564.
[7] M. Craig, G. Coulter, E. Dolan, et al., Nat. Commun. 10 (2019) 1–9.
[8] K. Chen, K.K. Mao, Y. Bai, et al., Chin. Chem. Lett. 33 (2022) 452–456.
[9] K.X. Wang, X.Y. Wang, Z.J. Li, et al., Nano Energy 77 (2020) 105162.
[10] M.P. Browne, Z. Sofer, M. Pumera, Energy Environ. Sci. 12 (2019) 41–58.
[11] Z.H. Kou, K.X. Wang, Z.B. Liu, et al., Small Struct. 3 (2022) 2100153.
[12] J.X. Yuan, X.D. Cheng, C.J. Lei, et al., Engineering 7 (2021) 1306–1312.
[13] X.Y. Lu, H.R. Xue, H. Gong, et al., Nano-Micro Lett. 12 (2020) 86.
[14] P. Shi, X.D. Cheng, S.L. Lyu, Chin. Chem. Lett. 32 (2021) 1210–1214.
[15] H. Chen, X. Liang, Y.P. Liu, et al., Adv. Mater. 32 (2020) 2002435.
[16] H.J. Song, H. Yoon, B. Ju, D.W. Kim, Adv. Energy Mater. 11 (2021) 2002428.
[17] J.B. Huang, Y. Jiang, T.Y. An, M.H. Cao, J. Mater. Chem. A 8 (2020) 25465–25498.
[18] M.S. Alnarabiji, O. Tantawi, A. Ramli, et al., Renew. Sust. Energy Rev. 114 (2019) 109326.
[19] J. Jiang, F.F. Sun, S. Zhou, et al., Nat. Commun. 9 (2018) 2885.
[20] Y. Meng, G. Ni, X. Jin, J. Peng, Q.Y. Yan, Mater. Today Nano 12 (2020) 100095.
[21] Q. Wang, X. Huang, Z.L. Zhao, et al., J. Am. Chem. Soc. 142 (2020) 7425–7433.
[22] K. Fominykh, J. Feckl, J. Sicklinger, et al., Adv. Funct. Mater. 24 (2014) 3123–3129.
[23] Y.L. Ma, X. Wang, X.D. Sun, et al., Inorg. Chem. Front. 5 (2018) 1199–1206.
[24] P. Pattanayak, F. Papiya, V. kumar, N. Pramanik, P.P. Kundu, Sustain. Energy Fuels 3 (2019) 1808–1826.
[25] W. Yuan, C. Li, M. Zhao, et al., Electrochim. Acta 342 (2020) 136118.
[26] N.A. Khan, N. Rashid, M. Junaid, et al., ACS Appl. Energy Mater. 2 (2019) 3587–3594.
[27] L. Zhao, Y. Zhang, Z.L. Zhao, et al., Nat. Sci. Rev. 7 (2020) 27–36.
[28] W. Gao, Z.M. Xia, F.X. Cao, et al., Adv. Funct. Mater. 28 (2018) 1706056.
[29] Y.N. Wang, F. Cao, W.W. Lin, et al., J. Mater. Chem. A 7 (2019) 17834–17841.
[30] S.Y. Gong, A.Q. Wang, Y. Wang, et al., ACS Appl. Nano Mater. 3 (2020) 597–607.
[31] A.C. Pebley, E. Decolvenaere, T.M. Pollock, M.J. Gordon, Nanoscale 9 (2017) 15070–15082.
[32] Y. Liu, L. Bai, T. Li, et al., Appl. Surf. Sci. 577 (2022) 151952.
[33] Z. Qiu, Y. Ma, T. Edvinsson, Nano Energy 66 (2019) 104118.
[34] F. Cao, G.X. Pan, Y.J. Zhang, X.H. Xia, Chin. Chem. Lett. 31 (2020) 2230–2234.
[35] J.H. Jang, J. Kwon, S.R. Lee, K. Char, M. Kim, Appl. Phys. Lett. 100 (2012) 172101.
[36] X.L. Huang, M. Wang, R.C. Che, J. Mater. Chem. A 2 (2014) 9656.
[37] E.C. Dickey, V.P. Dravid, P.D. Nellist, et al., Microsc. Microanal. 3 (1997) 443–450.
[38] G. Evmenenko, T.T. Fister, F.C. Castro, et al., Phys. Chem. Chem. Phys. 21 (2019) 8897–8905.
[39] H.L. Xin, A. Vojvodic, J. Voss, J.K. Nørskov, F. Abild-Pedersen, Phys. Rev. B 89 (2014) 115114.
[40] J.K. Nørskov, T. Bligaard, J. Rossmeisl, C.H. Christensen, Nat. Chem. 1 (2009) 37–46.